

Dynamical origins of heat capacity changes in enzyme catalysed reactions

Authors:

Marc W van der Kamp^{1,2†*}, Erica J. Prentice^{3†}, Kirsty L. Kraakmann³, Michael Connolly²,
Adrian J. Mulholland^{2*} & Vickery L. Arcus^{3*}

Affiliations:

¹School of Biochemistry, Biomedical Sciences Building, University Walk, University of
Bristol, BS8 1TD, UK.

²Centre of Computational Chemistry, School of Chemistry, Cantock's Close, University of
Bristol, BS8 1TD, UK.

³School of Science, University of Waikato, Hamilton, New Zealand.

[†] These authors contributed equally to this work.

^{*} Corresponding authors email addresses: marc.vanderkamp@bristol.ac.uk,
adrian.mulholland@bristol.ac.uk, varcus@waikato.ac.nz

Abstract

Heat capacity changes are emerging as essential for explaining the temperature dependence of enzyme-catalysed reaction rates. This has important implications for enzyme kinetics, thermoadaptation and evolution, but the physical basis of these heat capacity changes is unknown. Here we show by a combination of experiment and simulation, for two quite distinct enzymes (dimeric ketosteroid isomerase and monomeric alpha-glucosidase), that the activation heat capacity change for the catalysed reaction can be predicted through atomistic molecular dynamics simulations. The simulations reveal subtle and surprising underlying dynamical changes: tightening of loops around the active site is observed as expected, but crucially, changes in energetic fluctuations are evident across the whole enzyme including important contributions from oligomeric neighbours and domains distal to the active site. This has general implications for understanding enzyme catalysis and demonstrating a direct connection between functionally important microscopic dynamics and macroscopically measurable quantities.

A critical variable for the rate of a reaction is temperature. For uncatalyzed chemical reactions, the rate of reaction typically increases exponentially with increasing temperature, as described by the Arrhenius and Eyring equations^{1,2}. In reactions catalysed by enzymes, the effects of temperature are complex and include (often opposing) contributions from active site geometry and reactivity, protein stability, conformational changes and temperature-dependent regulation. Changes in temperature can also potentially affect features of the enzyme catalysed reaction outside the chemical step such as substrate binding, product release and conformational changes. Despite these complexities, enzymes generally show a characteristic temperature profile including an optimum temperature (T_{opt}) for activity above which rates decline with increasing temperature. The decline in rate above T_{opt} cannot simply be explained by enzyme unfolding at higher temperatures and deviations from Eyring behaviour are also often seen at temperatures below T_{opt} ³⁻⁵. We recently developed macro-molecular rate theory (MMRT)^{6,7}, which explains the temperature dependence of enzymes including an intrinsic T_{opt} in the absence of denaturation by introducing the concept of heat capacity changes along the reaction coordinate: the heat capacity (C_p) for the enzyme–substrate complex is generally larger than C_p for the enzyme-transition state complex, in enzymes for which the chemical reaction is rate limiting. Hence, the activation heat capacity, ΔC_p^\ddagger , for the enzyme-catalysed reaction is generally negative (Fig. 1a; in case product release instead of chemical reaction is rate limiting, a small positive heat capacity for reaction is possible⁸). We have demonstrated that this accounts for the curvature observed in Eyring plots for a number of enzymes⁶.

ΔC_p^\ddagger is a statistical thermodynamic property for the catalysed reaction that describes the difference in heat capacity between the thermodynamic ensemble in the ground state and that at the transition state. It can be determined experimentally⁹, and can also be calculated from the variance in enthalpy at equilibrium for each of these states¹⁰:

$$\Delta C_p^\ddagger = \frac{\Delta \langle \partial H^2 \rangle^\ddagger}{k_B T^2} \quad (1)$$

In principle, atomistic molecular dynamics simulations at equilibrium can provide a distribution of enthalpies from which the variance $\langle \partial H^2 \rangle$ (the mean squared fluctuation in the

enthalpy) may be calculated. To do so, the ensemble for the enzyme-substrate complex and separately, that for the enzyme transition state complex, should be simulated.

Here, we experimentally determine the value for ΔC_p^\ddagger from the temperature dependence of the rate in the absence of enzyme denaturation for two quite different enzymes: the small, dimeric ketosteroid isomerase (KSI) and the large, monomeric α -glucosidase MalL (Fig. 1). In parallel, we employ extensive MD simulations (10 μ s per enzyme) to obtain heat capacity differences between two states along the reaction pathway. KSI is a very well-studied enzyme that is involved in steroid biosynthesis and degradation: it performs two consecutive proton transfers to shift the position of a C=C double bond¹¹ (Supplementary Fig. 1). MalL is a large α -glucosidase: it hydrolyses terminal non-reducing (1 \rightarrow 6)-linked α -glucose residues in a two-step reaction, releasing α -glucose¹² (Supplementary Fig. 2). Previously, we have shown by experiment that there is a large change in heat capacity for this enzyme-catalysed reaction and that single point mutations can dramatically alter the temperature dependence of the rate by altering the heat capacity of either the enzyme-substrate complex or the enzyme-transition state complex⁷.

Activation heat capacities from simulations and experiment are in good agreement. This shows that prediction of activation heat capacity for enzymes is feasible by simulations, opening a new route to predicting and engineering optimum temperatures for enzyme activities. Further, the simulations provide an atomically detailed picture of the dynamical differences between transition state and Michaelis complexes that gives rise to this behaviour, revealing complex, and intriguing changes in dynamics across the whole enzyme structure. We thus use simulation, for the first time, to interpret the ΔC_p^\ddagger obtained from macroscopic kinetics measurements in terms of detailed contributions at the atomistic level, providing a link between enzyme structural and energetic molecular fluctuations to its function and thermostability.

Results

ΔC_p^\ddagger determined by experiment

As shown previously^{6,7}, ΔC_p^\ddagger can be determined by fitting the $\ln(\text{rate})$ -versus-temperature plot using macromolecular rate theory (MMRT). For MalL, curvature in this plot is very significant (Fig. 1d), and unrelated to unfolding⁵. This leads to a negative ΔC_p^\ddagger value of $-11.6 \pm 0.4 \text{ kJ.mol}^{-1}.\text{K}^{-1}$. For KSI, the curvature is less extreme, but still obvious, leading to a small negative ΔC_p^\ddagger of $-0.86 \pm 0.1 \text{ kJ.mol}^{-1}.\text{K}^{-1}$ (Fig. 1c). An important consequence of the ΔC_p^\ddagger values of for each enzyme is the position of the optimum temperature (T_{opt}) for activity as these parameters are correlated. For example, the large negative ΔC_p^\ddagger value for MalL dictates the position of T_{opt} at 320 K whereas the much smaller ΔC_p^\ddagger value for KSI places the T_{opt} well above 320 K (in absence of protein unfolding). Similarly, the significant curvature of the MalL temperature dependence means that at lower temperatures, the rate approaches zero much faster for MalL when compared to KSI.

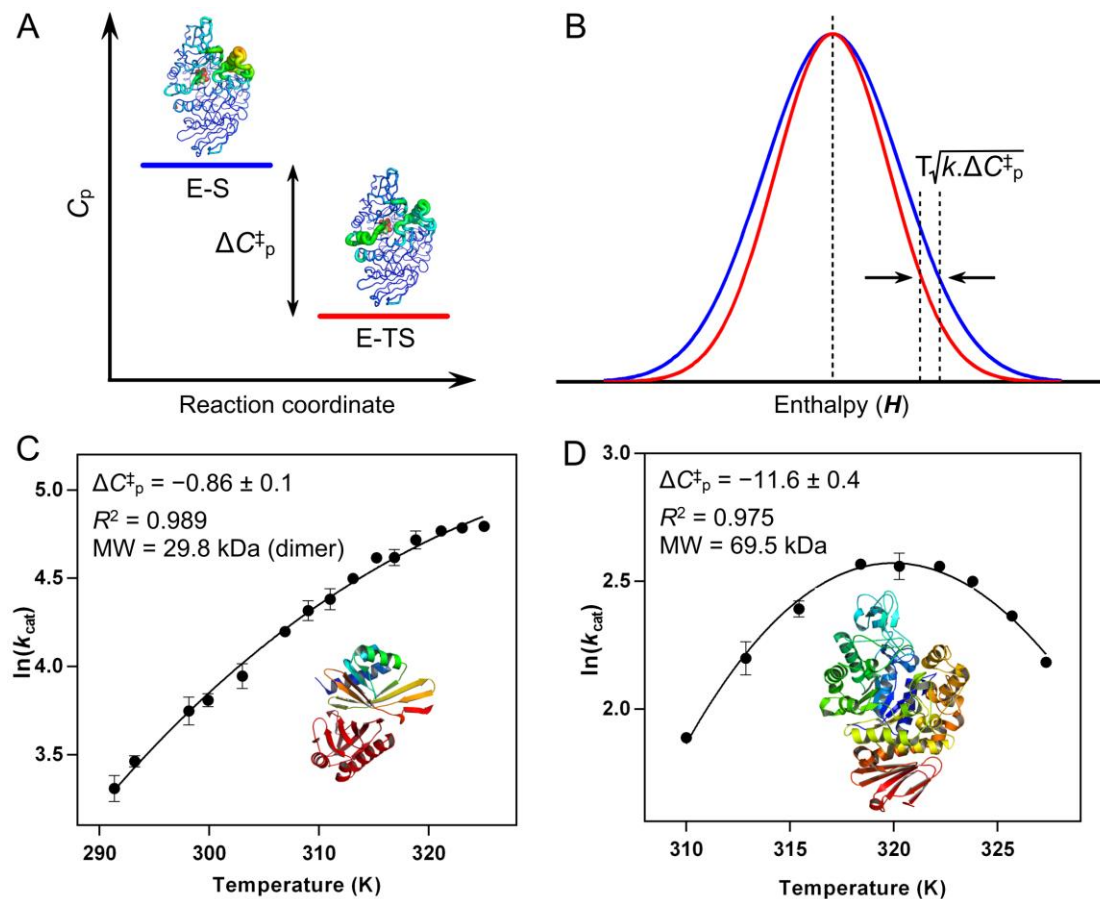


Figure 1: Basis of a negative ΔC_p^\ddagger and its determination through experiment. **A**, Conceptual depiction of a difference in C_p between the enzyme-substrate (E-S) and enzyme-transition state (E-TS) complexes along a reaction, resulting in a negative ΔC_p^\ddagger . **B**, Conceptual depiction of differences in enthalpy distribution at the E-TS (red) and the E-S states (blue). Arrows indicate the inflection points (at $\mu+\sigma$), and the difference defines ΔC_p between the two states according to the formula given (see equation (1)). **C-D**, Experimentally determined ΔC_p^\ddagger values ($\text{kJ}\cdot\text{mol}^{-1}\cdot\text{K}^{-1} \pm \text{SE}$) for the temperature-dependent rates of KSI (**C**) and Mall (**D**). Data is fit with MMRT (see Methods). Error bars, where visible, represent the SD of three replicates. Figures of KSI and Mall are to scale.

Heat capacity differences from simulation

Heat capacity differences for enzyme catalyzed reactions can be calculated from $\Delta\langle\partial H^2\rangle^\ddagger$ (eq. (1)). To measure $\Delta\langle\partial H^2\rangle^\ddagger$ from simulation, there are two main challenges: a) the amount of sampling required for the system to define the enthalpy variance, and b) an accurate and

consistent representation of the reactant state (Michaelis complex) and the transition state. A statistical thermodynamic analysis of a 1 ms molecular dynamics (MD) simulation of the bovine pancreatic trypsin inhibitor indicated that 10s of μ s of simulation may be needed to converge the heat capacity difference between two conformational states¹³. Sampling on the order of (at least) μ s is thus expected to be required for reliable identification of heat capacity differences. Such sampling is now routinely feasible with a ‘molecular mechanics’ description of the atoms and their interactions. We thus compare two states, A and B (Fig. 1a), and the difference in heat capacity between these states can be determined by:

$$\Delta C_{A,B} = \frac{\langle \delta H_B^2 \rangle - \langle \delta H_A^2 \rangle}{k_B T^2} \quad (2)$$

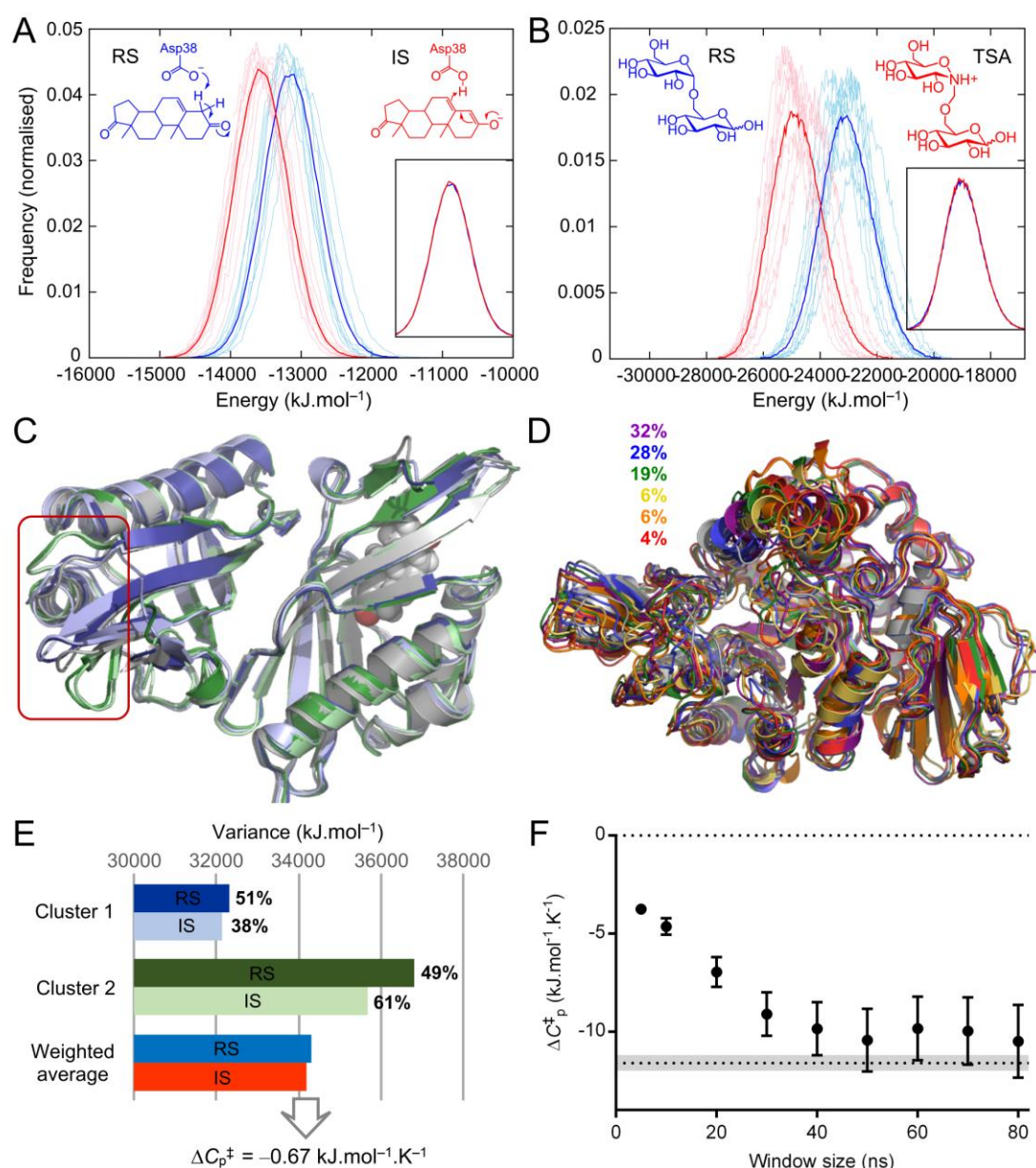
To sample the conformational dynamics of the reactant (E-S or RS) and ‘transition state’ (E-TS) enzyme complexes consistently, electronically unstable states (e.g. with half-formed bonds involving enzyme residues) should be avoided for the ‘transition state’ representation. We thus use molecular species that are representative for the transition state (i.e. transition state analogues), and predict that these will show a similar heat capacity change from the reactant state. This prediction has been demonstrated experimentally for human 5'-methylthioadenosine phosphorylase⁹. For KSI, a charged enediolate intermediate is formed after the first proton transfer, and this is the key species stabilised by the enzyme for catalysis of the reaction^{14,15}. We use this intermediate state as a proxy for the two enzyme-transition state complexes (one for each proton transfer) as the intermediate lies between the two transition states at similar energy. The substrate (5-androstene-3,7-dione) and intermediate complexes (Fig. 2a, Supplementary Fig. 1) were built based on KSI in complex with the inhibitor 5 α -estran-3,17-dione (PDB 1OHP). For Mall, we obtained an experimental X-ray structure co-crystallised with a stable transition state analogue (Supplementary Table 1; Supplementary Fig. 4) and use this to simulate the thermodynamics of the substrate isomaltose and a close analogue of the transition state species at the rate determining step¹⁶ (Fig. 2b; Supplementary Fig. 2).

A total of 5 μ s of MD simulation was run for KSI and MalL in both the substrate-bound and proxy TS representations over ten replicate simulations for each state (Supplementary Results). The force-field potential energy was used as an approximation for the system enthalpy, and was recalculated for the protein-ligand system without explicit water. Considering the *variance* of the enthalpy is the quantity required for C_p^\ddagger calculation (eq. (1)) and a *difference* in variance between two states is used to determine ΔC_p^\ddagger (eq. (2)) these approximations should be reasonable.

For KSI, the conformational space sampled is limited, with only two distinct structural clusters discernible. The difference between these clusters is in a small region in the unoccupied monomer (Fig. 2c). The H variance is significantly different between the clusters, however (Fig. 2e). For ΔC_p^\ddagger calculation, we thus calculate the variance of the clusters separately, with the total variance for each state being the average variance weighted by the cluster occupation (Fig. 2e).

MalL samples a larger conformational space than KSI, occupying and regularly switching between a number of structural clusters along the simulation trajectories, related primarily to changes in loops surrounding the active site (Figure 2d; Supplementary Results). Due to the presence of multiple conformational clusters, consideration of the system over the full simulation time overinflates the enthalpy variance. However, calculating variances for each cluster (as for KSI) does not take into account that frequent switches between the distinct conformational states will also contribute to the variance. In addition, several clusters are dominated by one state only (Supplementary Fig. 8). To be independent of clustering and account for switching between conformational substates, enthalpy variance was calculated using a moving window along the simulation trajectory for each simulation, and subsequent averaging. The ‘window’ for the moving average was varied between 5-80 ns and calculated ΔC_p^\ddagger values converge when the window size is between 40-80 ns (Figure 2f, Supplementary Table 3). Thus, the calculated ΔC_p^\ddagger values for MalL converge on a value of –

176 $10.0 \pm 1.7 \text{ kJ.mol}^{-1}.\text{K}^{-1}$ (using a window of 70 ns) which is within the error range of the
 177 experimentally determined ΔC_p^\ddagger value of $-11.6 \pm 0.4 \text{ kJ.mol}^{-1}.\text{K}^{-1}$.



178 $\Delta C_p^\ddagger = -0.67 \text{ kJ.mol}^{-1}.\text{K}^{-1}$

179 **Figure 2: Sampling and ΔC_p^\ddagger calculation in simulations.** A-B, Histograms of energies from
 180 50-500ns MD simulations for KSI (A) and MalL (B). Thin lines are individual runs, thick
 181 lines are the average of 10 runs. Insets show overlay of histograms for both states, and the
 182 structures indicate the species simulated (RS – reactant state; IS – intermediate state; TSA –
 183 transition state analogue). C, Representative structures for the two distinct conformational
 184 clusters present in the KSI simulations of both states (reactant state in blue and green,

intermediate state in pale blue and green, starting structure in light grey). Box highlights the region with structural differences. **D**, Representative structures for the 6 main conformational clusters in MalL reactant state simulations and their occupancies (starting structure in light grey). **E**, Variance in energies for the two clusters identified in the KSI simulations, with cluster occupancies (in %) and weighted average variance for both states. **F**, Convergence with moving average window size of ΔC_P^\ddagger values calculated for MalL, with value determined from experiment indicated by dotted line (with grey area indicating standard deviation).

Local and global contributions to ΔC_P^\ddagger

The observation that ΔC_P^\ddagger values calculated from extensive conformational sampling are in agreement with those determined experimentally allows meaningful analysis of the differences between the two ensembles. Striking results emerge from analysing contributions from different parts of the enzymes, by calculating ΔC_P^\ddagger values for parts of the structures (by recalculating energies and their variances for specific regions only; Fig. 3). Energy contributions from interactions with neighbouring regions are not included, and therefore one should not expect these ‘partial’ ΔC_P^\ddagger values to add up to the total value. They do, however, offer new quantitative insights. Conceptually, one may expect differences in partial ΔC_P^\ddagger values to align with regions that differ in flexibility. This is largely true for some small regions with clear differences in flexibility (e.g. residues 46-70 for KSI; residues 250-321 and 374-459 for MalL; see Fig. 3), but is not obvious throughout the structure, especially for larger regions. Crucially, differences in ΔC_P^\ddagger are distributed across the full protein structure, whereas significant differences in flexibility are limited to regions that interact with the ligand bound in the active site.

KSI, as a dimer, offers the opportunity to assess the dynamical role of the monomer that is distal to substrate turnover. The distal monomer of KSI is the main contributor to reduced ΔC_P^\ddagger at the TS (Figure 3A). Overall, the catalytic monomer contributes a positive ΔC_P^\ddagger ; the N- and C-terminal regions forming the back of the active site and more remote regions contribute

a positive ΔC_p^\ddagger , while helix 48-59 that closes over the active site opposite from the catalytic Asp38 rigidifies and contributes a negative ΔC_p^\ddagger . Implication of the non-catalytic chain as a significant contributor to negative ΔC_p^\ddagger points to an important role for the oligomer in the temperature dependence of the catalytic process. Enzyme oligomerization is common, indicating an evolutionary advantage¹⁷, however the functional purpose of these quaternary interactions is not well understood. If interactions are optimized to allow global contributions from changes in the distribution of vibrational modes across the multimer¹⁸, oligomerization may provide a means to tune the temperature dependence of rates through global contributions to the overall C_p change.

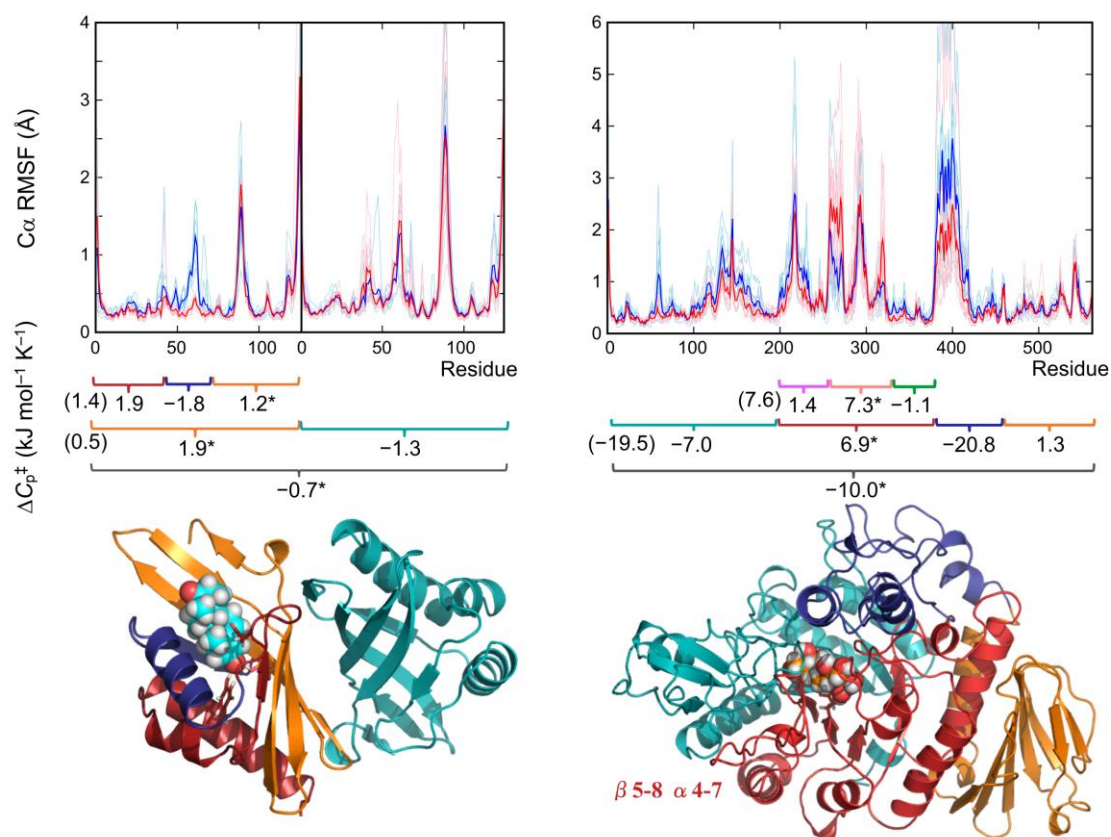


Fig. 3. Structural fluctuations and partial variances between reactant state and transition state analogue complexes. Top: root-mean square fluctuations from 50-500ns MD simulations for KSI (left) and MalL (right). Thin lines are individual runs, thick lines the average of 10 runs. Middle: calculated partial ΔC_p^\ddagger values for protein regions. Values

including contribution from the ligand are indicated (*). Bottom: illustration of KSI (left) and MalL (right) colored based on partial ΔC_p^\ddagger regions from top pane. Transition-state analogues shown in space-filling spheres.

The active site of MalL (and TIM barrel enzymes in general¹⁹) sits displaced to one side above the TIM barrel core, interacting with a half of the barrel comprising $\beta 5-8$ and $\alpha 4-7$ (Figure 3B). Analogous to the ligand bound chain of KSI, the catalytic half of the TIM barrel increases in C_p at the TS, while more remote protein components including the second TIM half barrel contribute to the overall negative ΔC_p^\ddagger . The lid domain, consisting of a helix-loop-helix extension above the barrel, contributes significantly to the overall reduction in C_p at the TS, consistent with a role shielding the active site from solvent at the catalytic step. The parallels between the KSI dimer and MalL barrel halves are especially noteworthy in that the TIM barrel is argued to have evolutionary origins as a dimer of $(\beta\alpha)_4$ units^{19,20}, the dynamical origins of which may still be discernible in the now fused structure.

Overall, these data indicate that the decrease of C_p between the enzyme-substrate and enzyme-TS complexes is not just a function of rigidification of elements around the active site, but significant contributions are also made by regions remote from the active site, including oligomeric partners.

Discussion

In enzyme catalysis, ΔC_p^\ddagger is emerging as a critical parameter for describing the temperature dependence of enzymatic rates, and as a consequence, for thermal adaptation in enzyme evolution^{6,7}. The capacity to predictably manipulate enzyme activity with temperature continues to be a sought-after goal in biotechnology²¹, but a lack of understanding of the principles governing thermal activity hampers the guided development of enzymes. The *in silico* replication of experimental ΔC_p^\ddagger values gives, for the first time, insight into the atomic-level details of C_p changes along the reaction coordinate which govern the temperature

dependence of enzyme rates. In turn, this provides a route to engineer temperature optima of enzymes: modifications in enzyme structure that change ΔC_p^\ddagger can be proposed and tested. Due to the difficulty of converging the difference in enthalpy variance that underlies ΔC_p^\ddagger , one cannot expect perfect quantitative agreement between simulation and experiment, but trends and, importantly, atomistic mechanistic details can be extracted.

In two distinct enzyme systems, contributions to reduced ΔC_p^\ddagger at the TS come from small domains surrounding the active site as well as domains distant from the catalytic centre. Rigidification of active site loops is expected as these regions may tighten around the transition state ensemble during catalysis. Unexpectedly, domains distal to the active site contribute significantly to the overall negative ΔC_p^\ddagger , offsetting positive contributions to ΔC_p^\ddagger around the active site (excluding the loops). This observation has implications for the biological importance of both enzyme mass and oligomerization. Previously, enzyme mass has been found to be correlated to catalytic efficiency, leading to the suggestion that vibrational modes (available through the large size of enzymes) act as an energy reservoir, a portion of which is available for catalysis⁶. Distal contributions to negative values of ΔC_p^\ddagger seen here provide evidence that the necessary changes in the distribution of vibrational modes that give rise to a negative ΔC_p^\ddagger are dispersed throughout the protein mass. Further, extension of this idea into auxiliary domains (MalL) and dimeric units (KSI) not directly involved with the reaction chemistry suggest that this ‘energy reservoir’ extends further than the catalytic domain. This assigns a significant functional role to distal domains regardless of proximity to the active site, suggesting a functional reason driving the evolution of these domains and interactions.

Methods

Cloning, protein expression, purification, and characterization. Cloning, expression, purification and activity assays of MalL were as described previously⁷. Co-crystallization of MalL with 0.5 mM 1-deoxynojirimycin was performed using hanging drop vapor diffusion at 18 °C. Crystals were flash cooled with cryoprotectant comprising of the crystallization mixture with 20 % glycerol for collection at the Australian Synchrotron (MX1). Molecular replacement was performed with the WT MalL apo structure (PDB 4M56)⁷ as the search model.

The KSI sequence (*Pseudomonas testosteroni*) with a C-terminal hexa-His tag was optimized for expression in *E. coli*. Expression was carried out over ~24 hours in Luria-Bertani broth at 28 °C. Purified KSI was obtained by a two-step immobilized metal affinity (IMAC)-gel filtration chromatography process. KSI activity was measured *in vitro* using a continuous enzyme assay following the isomerization of 19-nor-androst-5(10)-ene-3,17-dione at 248 nm in phosphate buffer (pH 7.0) for minimal pH change with temperature.

Experimental ΔC_p^\ddagger determination. Temperature vs. rate profiles were determined by measuring rates in a continuous assay at temperature intervals of 2-4 °C at saturating substrate concentrations. Temperature was controlled via a ThermoSpectronic single cell peltier, and independently checked before and after assays by thermocouple. Initial rates were measured over a period of 10 seconds to limit the effect of denaturation, if present, at elevated temperatures. Temperature profiles were fit with eq. 3 with reference temperature (T_0) set to $T_{opt} - 4$:

$$\ln(k) = \ln\left(\frac{k_B T}{h}\right) - \frac{[\Delta H_{T_0}^\ddagger + \Delta C_p^\ddagger(T - T_0)]}{RT} + \frac{[\Delta S_{T_0}^\ddagger + \Delta C_p^\ddagger \ln(T/T_0)]}{R} \quad (3)$$

where k = rate; k_B = Boltzmann constant; h = Planks constant; $\Delta H_{T_0}^\ddagger$ = Enthalpy at T_0 ; R = ideal gas constant; $\Delta S_{T_0}^\ddagger$ = entropy at T_0 . The transmission coefficient, κ , is assumed to be 1 for simplicity and is not included.

304

305 *MD simulation and analysis.* All simulations and analyses were performed using the Amber
 306 package and the ff99SB-ILDN protein force field. For KSI, PDB entry 1OHP was used with
 307 Asn38 mutated back to the wild-type Asp and either the substrate or intermediate of the KSI
 308 reaction (Fig. 2A) modelled in chain A (based on the co-crystallised inhibitor 5 α -estran-3,17-
 309 dione); chain B was left empty. General Amber FF (GAFF) parameters with charges from
 310 HF/6-31G(d) RESP fitting (RED server: <http://upjv.q4md-forcefieldtools.org/REDS/>) were
 311 used for the ligand. Asp38 was treated as protonated only for the intermediate state in chain A.
 312 Asp99 was protonated in both chains, with all other ionizable residues in their standard states.
 313 All three Histidines were singly protonated on N ϵ 2 and some Asn/His residue side-chains
 314 were rotated by 180° to obtain an optimal hydrogen bond network. For MalL, chain A from
 315 the 1-deoxynojirimycin bound structure obtained here (PDB entry 5WCZ) was used with
 316 missing atoms built in with COOT based on electron density where available. The substrate
 317 isomaltose was placed in the active site by overlay with PDB entry 3AXH (E277A MalL from
 318 *S. cerevisiae*; C α RMSD 0.84 Å) and simulated using GLYCAM (06j-1) parameters. The
 319 transition state analogue used in simulation was placed in the active site based on the
 320 modelled position of isomaltose and the position of 1-deoxynojirimycin in our co-crystal
 321 structure, and simulated using GLYCAM for the glucose unit, and GAFF (with HF/6-31G(d)
 322 RESP fitted charges) for the unit containing the protonated nitrogen. Asp63 and Glu371 were
 323 treated as protonated in both states, with the catalytic residues Asp199 unprotonated and
 324 Glu255 protonated (in line with the mechanism). Other ionizable residues were in their
 325 standard protonation states, with His161 singly protonated on N δ 1 and all other His on N ϵ 2.
 326 The preparation/equilibration protocol was as follows: solvation in a truncated octahedral of
 327 TIP4P(Ew) water molecules (keeping all crystallographic waters) with Na⁺ ions added to
 328 neutralize overall charge (ion positions randomized for each independent run), brief
 329 minimization followed by heating in 20ps to 300 K (KSI) or 320 K (MalL) with positional
 330 restraints on C α atoms (5 kcal mol⁻¹ Å⁻²), gradual release of restraints in 40 ps, equilibration

in the NPT ensemble for 1 ns. 500 ns production simulations were performed in the NVT ensemble with the Berendsen thermostat and loose temperature coupling (10 ps time constant). For both enzymes, restraints were used to maintain the Michaelis complex (with equivalent restraints on the IS or TSA states; Supplementary Methods). Analysis was performed using 10 ps snapshots from 50-500 ns of the simulations, with force-field energies re-calculated after stripping of solvent and ions. Clustering on the C α RMSD (excluding the highly flexible C-terminal residues 117-125 in KSI and the N-terminal residues 1-6 in MalL) was performed using the hierarchical agglomerative algorithm using a minimum cluster distance of 1.6 for KSI and 2.1 for MalL. C α RMSF was calculated using RMSD fitting to a running average coordinates from a time window of 10 ns.

Data availability. Coordinates and structure factors for MalL co-crystallised with 1-deoxynojirimycin are deposited in the PDB under accession number 5WCZ. Simulation input files are available from the Dryad Digital Repository (DOI code [to be inserted]).

References

- 1 Arrhenius, S. Über die Reaktionsgeschwindigkeit bei der Inversion von Rohrzucker durch Säuren. *Z Phys Chem* **4**, 226-248 (1889).
- 2 Eyring, H. The activated complex in chemical reactions. *J Chem Phys* **3**, 107-115 (1935).
- 3 Thomas, T. M. & Scopes, R. K. The effects of temperature on the kinetics and stability of mesophilic and thermophilic 3-phosphoglycerate kinases. *Biochemical Journal* **330**, 1087-1095 (1998).
- 4 Daniel, R. M. & Danson, M. J. A new understanding of how temperature affects the catalytic activity of enzymes. *Trends in Biochemical Sciences* **35**, 584-591 (2010).
- 5 Buchanan, C. L., Connaris, H., Danson, M. J., Reeve, C. D. & Hough, D. W. An extremely thermostable aldolase from *Sulfolobus solfataricus* with specificity for non-phosphorylated substrates. *Biochemical Journal* **3**, 563-570 (1999).

- 359 6 Arcus, V. L. *et al.* On the Temperature Dependence of Enzyme-Catalyzed Rates.
360 *Biochemistry* **55**, 1681-1688 (2016).
- 361 7 Hobbs, J. K. *et al.* Change in Heat Capacity for Enzyme Catalysis Determines
362 Temperature Dependence of Enzyme Catalyzed Rates. *ACS Chemical Biology* **8**,
363 2388–2393 (2013).
- 364 8 Nguyen, V. *et al.* Evolutionary drivers of thermoadaptation in enzyme catalysis.
365 *Science* **355**, 289-293 (2017).
- 366 9 Firestone, R. S., Cameron, S. A., Karp, J. M., Arcus, V. L. & Schramm, V. L. Heat
367 capacity changes for transition-state analogue binding and catalysis with human 5 '-
368 methylthioadenosine phosphorylase. *ACS Chemical Biology* **12**, 464-473 (2017).
- 369 10 Prabhu, N. V. & Sharp, K. A. Heat Capacity in Proteins. *Annual Review of Physical*
370 *Chemistry* **56**, 521-548 (2005).
- 371 11 Ha, N. C., Choi, G., Choi, K. Y. & Oh, B. H. Structure and enzymology of Delta5-3-
372 ketosteroid isomerase. *Curr Opin Struct Biol* **11**, 674-678 (2001).
- 373 12 Zechel, D. L. & Withers, S. G. Glycosidase Mechanisms: Anatomy of a Finely
374 Tuned Catalyst. *Accounts of Chemical Research* **33**, 11-18 (2000).
- 375 13 Fenley, A. T., Muddana, H. S. & Gilson, M. K. Entropy-enthalpy transduction caused
376 by conformational shifts can obscure the forces driving protein-ligand binding. *Proc*
377 *Natl Acad Sci U S A* **109** (2012).
- 378 14 van der Kamp, M. W., Chaudret, R. & Mulholland, A. J. QM/MM modelling of
379 ketosteroid isomerase reactivity indicates that active site closure is integral to
380 catalysis. *FEBS Journal* **280**, 3120-3131 (2013).
- 381 15 Fried, S. D., Bagchi, S. & Boxer, S. G. Extreme electric fields power catalysis in the
382 active site of ketosteroid isomerase. *Science* **346**, 1510-1514 (2014).
- 383 16 Cogoli, A. & Semenza, G. A probable oxocarbonium ion in the reaction mechanism
384 of small intestinal sucrase and isomaltase. *J Biol Chem* **250**, 7802-7809 (1975).
- 385 17 Ricard, J. & Noat, G. Catalytic efficiency, kinetic co-operativity of oligomeric
386 enzymes and evolution. *Journal of Theoretical Biology* **123**, 431-451 (1986).

- 387 18 Kim, T. H. *et al.* The role of dimer asymmetry and protomer dynamics in enzyme
388 catalysis. *Science* **355** (2017).
- 389 19 Wierenga, R. K. The TIM-barrel fold: a versatile framework for efficient enzymes.
390 *FEBS Letters* **492**, 193-198 (2001).
- 391 20 Höcker, B., Jürgens, C., Wilmanns, M. & Sterner, R. Stability, catalytic versatility
392 and evolution of the ($\beta\alpha$)₈-barrel fold. *Current Opinion in Biotechnology* **12**, 376-381
393 (2001).
- 394 21 Burton, S. G., Cowan, D. A. & Woodley, J. M. The search for the ideal biocatalyst.
395 *Nat Biotechnol* **20**, 37-45 (2002).

396

397 **Acknowledgments**

398 MWvdK is a BBSRC David Phillips Fellow (BB/M026280/1) and he and AJM thank the
399 BrisSynBio Synthetic Biology Research Centre for funding (BB/L01386X/1). EJP was
400 supported by a University of Waikato Doctoral Scholarship and VLA was supported by the
401 Marsden Fund of New Zealand (08-UOW-057). MC and AJM thank the EPSRC Centre for
402 Doctoral Training in Theory and Modelling in Chemical Sciences (EP/L015722/1).

403

404 **Author contributions**

405 MWvdK devised simulation and analysis; MWvdK and EJP performed simulations and
406 analysis, assisted by MC; EJP and KLK performed experiments; MWvdK, EJP, AJM and
407 VLA analysed and interpreted results, and wrote the manuscript. MWvdK and EJP
408 contributed equally to this work.